# Trans-rectal ultrasound-coupled near-infrared optical tomography of the prostate Part I: Simulation

Guan Xu,[1] Daqing Piao,[1*] Cameron H. Musgrove,[2] Charles F. Bunting, [1]
Hamid Dehghani [3]

[1] *School of Electrical and Computer Engineering, Oklahoma State University, Stillwater, OK, 74078-5032, USA*
[2] *Sandia National Laboratories, Albuquerque, NM, 87155-1330, USA*
[3] *School of Physics, University of Exeter, Exeter, UK, EX4 4QL*
**Corresponding Author: daqing.piao@okstate.edu*

**Abstract:** We investigate the feasibility of trans-rectal optical tomography of the prostate using an endo-rectal near-infrared (NIR) applicator that is to be integrated with a trans-rectal ultrasound (TRUS) probe. Integration with TRUS ensures accurate endo-rectal positioning of the NIR applicator and the utility of using TRUS spatial *prior* information to guide NIR image reconstruction. The prostate NIR image reconstruction is challenging even with the use of spatial *prior* owing to the anatomic complexity of the imaging domain. A hierarchical reconstruction algorithm is developed that implements cascaded initial-guesses for nested domains. This hierarchical image reconstruction method is then applied to evaluating a number of NIR applicator designs for integration with a sagittal TRUS transducer. A NIR applicator configuration feasible for instrumentation development is proposed that contains one linear array of optodes on each lateral side of the sagittal TRUS transducer. The performance of this NIR applicator is characterized for the recovery of single tumor mimicking lesion as well as dual targets in the prostate. The results suggest a strong feasibility of trans-rectal prostate imaging by use of the endo-rectal NIR/US probe.



**OCIS codes:** (170.3880) Medical and biological imaging; (170.6960) Tomography; (170.7230) Urology.

## References and links

1. A. Jemal, R. Siegel, E. Ward, T. Murray, J. Xu, and M. J. Thun, "Cancer statistics, 2007," CA Cancer J. Clin. **57**, 43-66 (2007).
2. T. J. Polascik, J. E. Oesterling, and A. W. Partin, "Prostate specific antigen: a decade of discovery--what we have learned and where we are going," J. Urol. **162**, 293-306 (1999).
3. G. D. Grossfeld and P. R. Carroll, "Prostate cancer early detection: a clinical perspective," Epidemiol Rev. **23**, 173-80 (2001).
4. T. A. Stamey, M. Caldwell, J. E. McNeal, R. Nolley, M. Hemenez, and J. Downs, "The prostate specific antigen era in the United States is over for prostate cancer: what happened in the last 20 years?," J. Urol. **172**, 1297-1301 (2004).
5. C. R. Pound, A. W. Partin, M. A. Eisenberger, D. W. Chan, J. D. Pearson, and P. C. Walsh, "Natural history of progression after PSA elevation following radical prostatectomy," JAMA. **281**, 1591-1597 (1999).
6. A. C. Loch, A. Bannowsky, L. Baeurle, B. Grabski, B. König, G. Flier, O. Schmitz-Krause, U. Paul, and T. Loch, "Technical and anatomical essentials for transrectal ultrasound of the prostate," World J. Urol. **25**, 361-366 (2007).
7. A. Bill-Axelson, L. Holmberg, M. Ruutu, et al. "Radical prostatectomy versus watchful waiting in early prostate cancer," N. Engl. J. Med. **352**, 1977-1984 (2005).
8. B. Spajic, H. Eupic, D. Tomas, G. Stimac, B. Kruslin, and O. Kraus, "The incidence of hyperechoic prostate cancer in transrectal ultrasound-guided biopsy specimens," Urology **70**, 734-737 (2007).

#99968 - $15.00 USD Received 8 Aug 2008; revised 13 Oct 2008; accepted 14 Oct 2008; published 15 Oct 2008

9. K. Shinohara, T. M. Wheeler, and P. T. Scardino, "The appearance of prostate cancer on transrectal ultrasonography: correlation of imaging and pathological examinations," J. Urol. **142**, 76-82 (1989).
10. C. R. Porter, "Does the number of prostate biopsies performed affect the nature of the cancer identified?" Nat. Clin. Pract. Urol. **4**, 132-133 (2007).
11. V. Scattoni, A. Zlotta, R. Montironi, C. Schulman, P. Rigatti, and F. Montorsi, "Extended and saturation prostatic biopsy in the diagnosis and characterisation of prostate cancer: a critical analysis of the literature," Eur. Urol. **52**,1309-1322 (2007).
12. B. Tromberg, J. Coquoz, O. Fishkin, J. B. Pham, T. Anderson, E. R. Butler, J. Cahn, M. Gross, J. D. Venugopalan, and D. Pham, "Non-invasive measurements of breast tissue optical properties using frequency-domain photon migration," Phil. Trans. R. Soc. Lond. B **352**, 661-668 (1997).
13. B. W. Pogue, S. P. Poplack, T.O. McBride, W. A. Wells, K. S. Osterman, U. L. Osterberg, and K. D. Paulsen," Quantitative hemoglobin tomography with diffuse near-infrared spectroscopy: pilot results in the breast," Radiology **218**, 261-266 (2001).
14. V. Ntziachristos and B. Chance, "Probing physiology and molecular function using optical imaging: applications to breast cancer," Breast Cancer Res. **3**, 41-46 (2001).
15. R. Choe, A. Corlu, K. Lee, T. Durduran, S. D. Konecky, M. Grosicka-Koptyra, S. R. Arridge, B. J. Czerniecki, D. L. Fraker, A. DeMichele, B. Chance, M. A. Rosen, and A. G. Yodh, "Diffuse optical tomography of breast cancer during neoadjuvant chemotherapy: a case study with comparison to MRI," Med. Phys. **32**, 1128-1139 (2005).
16. M. A. Franceschini, K. T. Moesta, S. Fantini, G. Gaida, E. Gratton, H. Jess, W. W. Mantulin, M. Seeber, P. M. Schlag, and M. Kaschke, "Frequency-domain techniques enhance optical mammography: initial clinical results," Proc. Nat. Acad. Sci. USA **94**, 6468-6473 (1997).
17. Q. Zhu, E. B. Cronin, A. A. Currier, H. S. Vine, M. Huang, N. Chen, and C. Xu, "Benign versus malignant breast masses: optical differentiation with US-guided optical imaging reconstruction," Radiology **237**, 57-66 (2005).
18. S. A. Bigler, R. E. Deering, and M. K. Brawer, "Comparison of microscopic vascularity in benign and malignant prostate tissue," Hum. Pathol. **24**, 220-226 (1993).
19. J. H. Ali , W. B. Wang , M. Zevallos, and R. R. Alfano , "Near infrared spectroscopy and imaging to probe differences in water content in normal and cancer human prostate tissues," Technol. Cancer Res. Treat. **3**, 491-497 (2004).
20. M. R. Arnfield , J. D. Chapman, J. Tulip , M. C. Fenning, and M. S. McPhee , "Optical properties of experimental prostate tumors in vivo," Photochem. Photobiol. **57**, 306-311 (1993).
21. T. C. Zhu, A. Dimofte, J. C. Finlay, et al. "Optical properties of human prostate at 732 nm measured in mediated photodynamic therapy," Photochem. Photobiol. **81**, 96-105 (2005).
22. T. Svensson, S. Andersson-Engels, M. Einarsdóttír, and K. Svanberg, "In vivo optical characterization of human prostate tissue using near-infrared time-resolved spectroscopy," J. Biomed. Opt. **12**, 014022 (2007).
23. M. Goel, H. Radhakrishnan, H. Liu, et al. "Application of near infrared multi-spectral CCD imager system to determine the hemodynamic changes in prostate tumor," in *OSA Biomedical Topical Meetings* (Optical Society of America, 2006), paper SH10.
24. H. Liu, Y. Song, K. L. Worden, X. Jiang, A. Constantinescu, and R. P. Mason, "Noninvasive investigation of blood oxygenation dynamics of tumors by near-infrared spectroscopy," Appl. Opt. **39**, 5231-43 (2000).
25. X. Zhou and T. C. Zhu, "Image reconstruction of continuous wave diffuse optical tomography (DOT) of human prostate," in *Proceedings of the COMSOL Users Conference* (2006).
26. S. L. Jacques and M. Motamedi, "Tomographic needles and catheters for optical imaging of prostatic cancer," Proc. SPIE **2395**, 111-118 (1995).
27. C. Li, R. Liengsawangwong, H. Choi, and R. Cheung , "Using *a priori* structural information from magnetic resonance imaging to investigate the feasibility of prostate diffuse optical tomography and spectroscopy: a simulation study," Med. Phys. **34**, 266-274 (2007).
28. C. Musgrove, C. F. Bunting, H. Dehghani, B. W. Pogue, and D. Piao, "Computational aspects of endoscopic near-infrared optical tomography: initial investigations," Proc. SPIE **6343**, 643409 (2007)
29. D. Piao, H. Xie, W. Zhang, G. Zhang, C. H. Musgrove, C. F. Bunting, H. Dehghani, B. W. Pogue, and S. N. Vemulapalli, "Near-infrared optical tomography: endoscopic imaging approach," Proc. SPIE **6431**, 643103 (2007).
30. H. Dehghani, C. M. Carpenter, P. K. Yalavarthy, B. W. Pogue, and J. P. Culver, "Structural *a priori* information in near-infrared optical tomography," Proc. SPIE **6431**, 64310B1 (2007).
31. Q. Zhu, T. Durduran, V. Ntziachristos, M. Holboke, and A. G. Yodh, "Imager that combines near-infrared diffusive light and ultrasound," Opt. Lett. **24**, 1050-1052 (1999).
32. M. J. Holboke, B. J. Tromberg, X. Li, N. Shah, J. Fishkin, D. Kidney, J. Butler, B. Chance, and A. G. Yodh, "Three-dimensional diffuse optical mammography with ultrasound localization in a human subject," J. Biomed. Opt. **5**:237-47 (2000).
33. B. W. Pogue, S. Geimer, T. O. McBride, S. Jiang, U. L. Osterberg, and K. D. Paulsen, "Three-dimensional simulation of near-infrared diffusion in tissue: boundary condition and geometry analysis for finite-element image reconstruction," Appl. Opt. **40**, 588-600 (2001).

#99968 - $15.00 USD Received 8 Aug 2008; revised 13 Oct 2008; accepted 14 Oct 2008; published 15 Oct 2008

34. M. Schweiger, S. R. Arridge, and D. T. Delpy, "Application of the finite-element method for the forward and inverse models in optical tomography," J. Math. Imag. Vision **3**, 263-283 (1993).
35. J. J. More, "Levenberg--Marquardt algorithm: implementation and theory," in *Numerical Analysis*, (Springer Berlin / Heidelberg, 1978), pp. 105-116.
36. X. Yu, G. Chen, and S. Cheng, "Dynamic learning rate optimization of the backpropagation algorithm," IEEE Trans. Neural Netw. **6**, 669-677 (1995).
37. D. Shen, Y. Zhan, and C. Davatzikos, "Segmentation of prostate boundaries from ultrasound images using statistical shape model," IEEE Tran. Med. Imaging **22**, 539-55 (2003).
38. M. Schweiger, S. R. Arridge, O. Dorn, A. Zacharopoulos, and V. Kolehmainen, "Reconstructing absorption and diffusion shape profiles in optical tomography using a level set technique," Opt. Lett. **31**, 471-473 (2006).
39. V. Kolehmainen, S. R. Arridge, W. R. B. Lionheart, M. Vauhkonen, and J. P. Kaipio, "Recovery of region boundaries of piecewise constant coefficients of an elliptic PDE from boundary data," Inverse Probl. **15**, 1375-1391 (1999).
40. V. Kolehmainen, M. Vauhkonen, J. P. Kaipio, and S. R. Arridge, "Recovery of piecewise constant coefficients in optical diffusion tomography," Opt. Express **7**, 468-480 (2000).
41. V. Kolehmainen, S. R. Arridge, M. Vauhkonen, and J. P. Kaipio, "Simultaneous reconstruction of internal tissue region boundaries and coefficients in optical diffusion tomography," Phys. Med. Biol. **45**, 3267-3284 (2000).
42. S. Srinivasan, B. W. Pogue, H. Dehghani, S. Jiang, X. Song, and K. D. Paulsen, "Improved quantification of small objects in near-infrared diffuse optical tomography," J. Biomed. Opt. **9**, 1161-1171 (2004).
43. P. K. Yalavarthy, H. Dehghani, B. W. Pogue, and K. D. Paulsen, "Critical computational aspects of near infrared circular tomographic imaging: Analysis of measurement number, mesh resolution and reconstruction basis," Opt. Express **14**, 6113-6127 (2006).
44. H. Shan, N. Pantong, J. Su, H. Liu, and M. V. Klibanov, "Globally convergent reconstruction algorithm for diffusion tomography of prostate," in *Biomedical Optics/Digital Holography and Three-Dimensional Imaging/Laser Applications to Chemical, Security and Environmental Analysis* on CD-ROM (The Optical Society of America, Washington, DC, 2008), paper BSuE33.
45. A. M. Wise, T. A. Stamey, J. E. McNeal, and J. L. Clayton, "Morphologic and clinical significance of multifocal prostate cancers in radical prostatectomy specimens," Urology **60,** 264-9 92002).
46. G. J. Miller and J. M. Cygan, "Morphology of prostate cancer: the effects of multifocality on histological grade, tumor volume and capsule penetration," J. Urol. **152**(5 Pt 2), 1709-13 (1994).

## 1. Introduction

Prostate cancer is the second most commonly diagnosed cancer and the second leading cause of cancer deaths in American men [1]. Prostate cancer screening is performed by measurement of serum prostate-specific antigen (PSA) [2], digital rectal examination (DRE), and in many cases a combination of both tests [3]. The introduction of PSA test contributed to substantially increased detection rate of organ-confined prostate cancer or considerable stage migration [4]. However, PSA is not a specific indicator of prostate malignancy and post-treatment tumor recurrence, except after radical prostatectomy [5]. A clearly increased serum PSA value (>20 ng/ml) may indicate the presence of a prostate carcinoma at a very high probability [6]. In the gray zone between 4 and 10 ng/ml the tissue marker PSA is frequently influenced by benign alterations, so that it is not possible, on the basis of the PSA value alone, to differentiate between benign and malignant cases [6, 7]. DRE can often distinguish between prostate cancer and non-cancerous conditions; it may also detect prostate cancers having normal PSA levels. However, palpation during a DRE is subjective, insensitive, and more than half of all prostate cancers detected are not palpable [3]. When the suspicion of prostate cancer is raised by abnormal PSA and/or DRE, the diagnosis is made by biopsy. The technique of trans-rectal ultrasound (TRUS) based trans-rectal prostate biopsy, carried out with a semi-automatic coil spring device and an 18-gauge needle, is to date considered as the gold standard [6].

Prostate neoplastic lesions may be identified on TRUS as being hypoechoic [8]. However at most 60% neoplastic lesions appear hypoechoic on TRUS while most of the remaining neoplastic lesions appear isoechoic [9]. The hypoechoic, cancer-suspicious areas may be histologically either benign or malignant [9]. The lack of TRUS specificity thereby prompts the practice of "systematic biopsy" of the prostate. The current trend is to use 10- to 12-core

#99968 - $15.00 USD Received 8 Aug 2008; revised 13 Oct 2008; accepted 14 Oct 2008; published 15 Oct 2008

biopsy with a preference in the peripheral zone, where most neoplastic lesions are found, as the initial biopsy strategy. It should be noted that the majority of biopsies are found to be negative, and in men with persistent suspicion of prostate cancer after several negative biopsies, more extensive protocols (>12 cores) up to saturation biopsy (24 cores) represent a necessary diagnostic procedure [10]. However, despite years of research, the exact number of biopsies to be taken is still largely unknown [11].

The need of having many biopsy-cores for systematic, yet random, tissue sampling of the prostate may be alleviated if the acoustic contrast that TRUS relies on is augmented with functional or "surrogate" markers of the prostate tumor such that the biopsy is directed to the malignant lesions. A functional imaging modality augmenting TRUS is certainly more desirable if it is non-ionizing and minimally-invasive as is TRUS. Optical tomography based on near-infrared (NIR) light could emerge as such a modality.

Near-infrared measurements of attenuation through tissue have demonstrated significant contrast gradients between blood and parenchymal tissue that is otherwise difficult to obtain [12-17]. The alteration of vascularity or the hemoglobin content in the tumor provides high intrinsic optical contrast between the tumor and benign tissues which has been well-demonstrated in breast cancer imaging [12-17]. When multi-spectral detection is engaged, NIR imaging is also capable of directly quantifying the chromorphore concentrations important for characterization of the malignancy [12-17]. In prostate, studies have shown vascular density gradient in malignant versus benign tissue specimens [18], and different water concentrations in cancerous and benign tissues *in vitro* [19]. Invasive NIR measurements of prostate have been conducted for experimental prostate tumors [20] and human prostate [21, 22]. Surface measurements of implanted prostate tumor have also been reported [23, 24]. All these studies demonstrate the potential of using NIR to detect and characterize prostate cancer. NIR diffuse optical measurement, performed interstitially, is also becoming an important tool for monitoring photodynamic therapy in prostate [21, 22, 25]. Prostate NIR imaging via trans-urethral probing had been analyzed and tested [26]. Recently, trans-rectal prostate NIR imaging has been investigated in simulation in the context of assisting MRI for treatment decision [27].

To our knowledge, experimental work on trans-rectal NIR tomography has not been performed except for our recent attempts [28, 29] which may be largely due to the challenge of fabricating a suitable trans-rectal applicator. Optical tomography typically needs 10s of channels of NIR optodes in order to achieve reasonable spatial resolution as a large tissue volume is being interrogated. The NIR illumination can be delivered by small diameter fibers, but the detection of weak scattered light is in favor of fibers of larger diameters and/or suitably larger numerical apertures. Unlike in breast NIR tomography where there is minimum spatial restriction for the optode configuration, trans-rectal applicator for NIR tomography has to deploy many optodes in a very compact space. This restriction could become more pronounced when trans-rectal NIR applicator is also to be combined with TRUS transducer. Since the depth of tissue interrogation by diffuse NIR light is roughly one-half of the source-detector separation for typical scattering-dominant biological tissue, reaching targets centimeters deep in prostate implies a NIR array of several centimeters in size. Such an NIR array is feasible for trans-rectal application if the optodes are arranged longitudinally, which should provide a sagittal-view in trans-rectal NIR imaging. The images obtained by trans-rectal NIR tomography alone would, however, be difficult to correlate with the anatomy. Unlike in breast imaging where the NIR applicator could be accurately positioned, accurate positioning of a trans-rectal NIR applicator with respect to the prostate is difficult which is due to the "blind" location of the prostate, slow NIR image reconstruction, and lack of anatomic details in NIR tomography images. It is thereby imperative to use a real-time morphological imaging modality concurrently with trans-rectal NIR tomography to provide a positioning guidance for NIR applicator in order to correlate the NIR tomography findings with the prostate anatomy. The structural information of the prostate can further be utilized as

#99968 - $15.00 USD Received 8 Aug 2008; revised 13 Oct 2008; accepted 14 Oct 2008; published 15 Oct 2008

the spatial *prior* [30] to improve the accuracy of NIR image reconstruction. Among the prostate imaging techniques, TRUS is perhaps the best modality for trans-rectal NIR tomography to combine owing to the operational similarity between these two modalities.

The diagnostic benefit of augmenting NIR contrast to US has been demonstrated in breast cancer detection [31, 32]. The methodology of combining NIR & US can certainly be extended from breast imaging to prostate imaging; nevertheless, the technique cannot be extended from imaging the breast to imaging the prostate without an NIR/US applicator suitable for trans-rectal manipulation. In this work, we demonstrate TRUS coupled trans-rectal optical tomography of the prostate. This work is reported in two consecutive papers. The Part-I paper, based on simulation, investigates designs of NIR tomography applicator suitable for integrating with a commercial TRUS transducer. A hierarchical NIR image reconstruction algorithm is developed for utilizing the TRUS structural *a priori* information which is then used to evaluate several NIR applicator configurations for integrating with a TRUS transducer. The Part-II paper implements the probe design suggested in Part-I, presents the instrumentation details of the TRUS coupled trans-rectal NIR tomography probe & system, and demonstrates TRUS-coupled trans-rectal NIR tomography of a canine prostate.

## 2. The geometry of trans-rectal NIR imaging and the utility of TRUS information

### *2.1 Configuration of sagittal trans-rectal NIR array for coupling with sagittal TRUS*

The TRUS is typically performed in bi-plane (sagittal and transverse) for prostate imaging. The sagittal and transverse views are switched during prostate imaging, but for biopsy procedure, the firing of the spring-loaded needle is monitored in the sagittal plane wherein the needle trajectory may be accurately marked. We have acquired a bi-plane TRUS probe (Aloka UST-672-5/7.5) as is shown in Fig. 1(a), which has a proximal sagittal transducer window of 60mm×10mm and a distal transverse transducer window of 120°×10mm. The cylindrical TRUS probe has a maximum diameter of 20mm. Integrating NIR applicator to a TRUS probe implies that the dimension, particularly the radial one, of the NIR array is quite restricted. As discussed earlier, longer source-detector separation is needed to interrogate deeper targets; therefore the most feasible configuration of an NIR array may be through distributing a linear array of optode on each lateral side of the sagittal TRUS transducer, as illustrated in Fig. 1(b). Taking into account the mechanical structure necessary to support the optodes, the combined

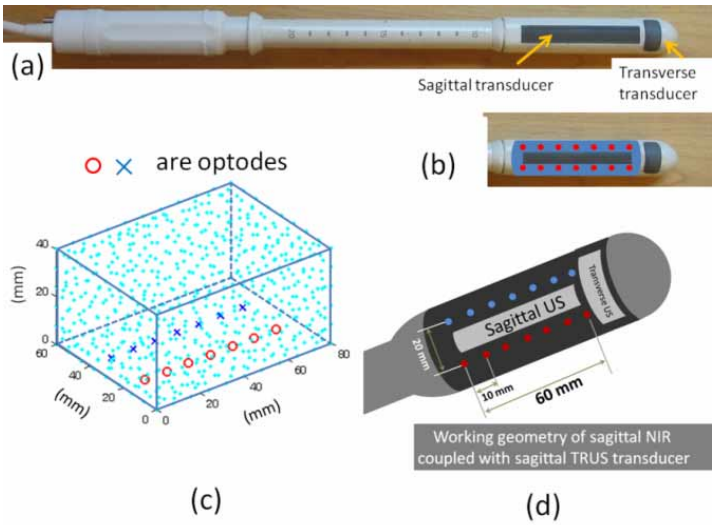


Fig. 1. (a) Photograph of a bi-plane TRUS transducer. (b) Configuration of an NIR array feasible for coupling with sagittal TRUS. (c) The NIR imaging geometry for the one depicted in (b). (d) Illustration of a trans-rectal probe that integrates NIR and US synergistically.

#99968 - $15.00 USD Received 8 Aug 2008; revised 13 Oct 2008; accepted 14 Oct 2008; published 15 Oct 2008

probe will likely have a radial size of at least a few millimeters larger than that of the original TRUS probe. NIR tomography has to use multimode fibers to detect weak diffuse light, and these multimode fibers must be delivered longitudinally before being side-fired. Bending the fiber is not a viable solution here for side-firing unless the fibers are passed inside the TRUS probe. The side-firing alternatively may however be realized by implementing micro-optical components, but the compact space inside or surrounding the probe may not accommodate a large number of such channels. A NIR array, which could couple with TRUS, may be configured by fabricating 7 fiber channels on each lateral side of the TRUS to span 60mm longitudinally as the TRUS does, and placing the optical channels 10mm apart. The NIR array must leave the 10mm-wide sagittal TRUS transducer unblocked; therefore a 20mm spacing of the NIR optodes from one lateral side to the other is perhaps needed. These considerations lead to the NIR array geometry shown in Fig. 1(c) where 14 optodes are spaced 10mm longitudinally and 20mm laterally. Fig. 1(d) illustrates an NIR/US probe if the sagittal NIR array can be fabricated synergistically with the TRUS probe.

*2.2 Forward and inverse methods for sagittal trans-rectal optical tomography*

The prostate and peripheral tissues are scattering-dominant in NIR [19-22]. We use the diffusion approximation to the radiative transport equation in frequency-domain [33]:

$$\nabla \cdot D(\vec{r})\nabla U(\vec{r},\omega) - (\mu_a + \frac{i\omega}{c})U(\vec{r},\omega) = -S(\vec{r},\omega) \tag{1}$$

where $U(\vec{r},\omega)$ is the photon fluence rate at position $\vec{r}$, $S(\vec{r},\omega)$ is the source, $\omega$ is the source modulation frequency, $c$ is the speed of light in the medium, $\mu_a$ is the absorption coefficient, and $D = [3(\mu_a + \mu_s')]^{-1}$ is the diffusion coefficient with $\mu_s'$ being the reduced or transport scattering coefficient. Finite-element method [34] is used to solve Equ. (1) under the Robin-type boundary condition [33]:

$$U(\vec{r}_0,\omega) + 2DA\hat{n}_0 \bullet \nabla U(\vec{r}_0,\omega) = 0 \tag{2}$$

where $\vec{r}_0$ is the boundary, $\hat{n}_0$ is the outward normal vector of the boundary and $A$ is the refractive index mismatch coefficient. The refractive indices used for air and tissue are 1 and 1.33 respectively, leading to $A$=2.82 as in [33].

The imaging volume is divided to 4 regions-of-interest (ROIs): the rectum wall, the peri-prostate tissue, the prostate, and the prostate tumor. The Jacobian (sensitivity) values are calculated for each ROI rather than each node which has the form of:

$$J = \begin{bmatrix} \frac{\partial \ln I_{11}}{\partial \mu_{a\_rect}} & \frac{\partial \ln I_{11}}{\partial \mu_{a\_peri}} & \frac{\partial \ln I_{11}}{\partial \mu_{a\_pros}} & \frac{\partial \ln I_{11}}{\partial \mu_{a\_lesi}} & \frac{\partial \ln I_{11}}{\partial \mu_{s\_rect}'} & \frac{\partial \ln I_{11}}{\partial \mu_{s\_peri}'} & \frac{\partial \ln I_{11}}{\partial \mu_{s\_pros}'} & \frac{\partial \ln I_{11}}{\partial \mu_{s\_lesi}'} \\ \frac{\partial \ln I_{12}}{\partial \mu_{a\_rect}} & \ddots & \ddots & \vdots & \vdots & \ddots & \ddots & \vdots \\ \vdots & \ddots & \ddots & \vdots & \vdots & \ddots & \ddots & \vdots \\ \frac{\partial \ln I_{77}}{\partial \mu_{a\_rect}} & \cdots & \cdots & \frac{\partial \ln I_{77}}{\partial \mu_{a\_lesi}} & \frac{\partial \ln I_{77}}{\partial \mu_{s\_rect}'} & \ddots & \ddots & \frac{\partial \ln I_{77}}{\partial \mu_{s\_lesi}'} \\ \frac{\partial \phi_{11}}{\partial \mu_{a\_rect}} & \frac{\partial \phi_{11}}{\partial \mu_{a\_peri}} & \frac{\partial \phi_{11}}{\partial \mu_{a\_pros}} & \frac{\partial \phi_{11}}{\partial \mu_{a\_lesi}} & \frac{\partial \phi_{11}}{\partial \mu_{s\_rect}'} & \cdots & \cdots & \frac{\partial \phi_{11}}{\partial \mu_{s\_lesi}'} \\ \frac{\partial \phi_{12}}{\partial \mu_{a\_rect}} & \ddots & \ddots & \vdots & \vdots & \ddots & \ddots & \vdots \\ \vdots & \ddots & \ddots & \vdots & \vdots & \ddots & \ddots & \vdots \\ \frac{\partial \phi_{77}}{\partial \mu_{a\_rect}} & \cdots & \cdots & \frac{\partial \phi_{77}}{\partial \mu_{a\_lesi}} & \frac{\partial \phi_{77}}{\partial \mu_{s\_rect}'} & \cdots & \cdots & \frac{\partial \phi_{77}}{\partial \mu_{s\_lesi}'} \end{bmatrix} \tag{3}$$

#99968 - $15.00 USD Received 8 Aug 2008; revised 13 Oct 2008; accepted 14 Oct 2008; published 15 Oct 2008

where $I_{ij}\ (i,j=1,2,...,7)$ and $\phi_{ij}\ (i,j=1,2,...,7)$ are the intensity and phase terms of $U(\vec{r},\omega)$, respectively. In Equ. 3, "rect", "peri", "pros", and "lesi" denote "rectum wall", "peri-prostate tissue", "prostate", and "prostate lesion", respectively.

The Levenberg-Marquart (LM) algorithm [35] governs the iterative recovery of the optical properties by updating the ROI-specific values of $\mu_a$ and $\mu_s'$ according to

$$x_{k+1} = x_k + \alpha \cdot [J^T(x_k)J(x_k) + \lambda I]^{-1} J^T(x_k)\Delta v(x_k) \tag{4}$$

where *x* is the array of parameters to be optimized, $\Delta v$ is the forward projection error and $\lambda$ is a penalty or regularization term. A small damping factor $\alpha$ in the range of (0, 1) is introduced in Equ. 4 to stabilize the convergence. It is shown that an empirically chosen $\alpha$ could make the LM algorithm more reliable and computationally more efficient [36].

*2.3 TRUS prior assisted finite-element mesh for trans-rectal NIR tomography reconstruction*

The TRUS prostate images which are available in open sources [37] are used for the simulation study. The TRUS image was first imported into a pre-processing software 3ds-MAX [Autodesk Inc] (shown in Fig. 2(a)). The 3ds-MAX provides very flexible geometry-deforming functions, with which a basic 3-D geometry of the prostate can be outlined manually. The finalized 3-D mesh of the prostate is then converted to COMSOL Multiphysics [COMSOL AB] compatible format (shown in Fig. 2(b)) using MeshToSolid [Syncode Inc]. The prostate tumor is then mimicked using a spherical shape to allow for flexibility of adjusting its size. The absorption and reduced scattering coefficients of the rectum, peri-prostate tissue, prostate and the tumor are assigned with values as suggested by literature [27]. Figure 3 illustrates one example of the completed FEM-mesh for trans-rectal optical tomography derived from a TRUS image, where x, y and z denoting the longitudinal, lateral and the depth coordinates, respectively. A typical mesh used for this work contains approximately 4000 nodes and 20000 linear tetrahedral elements.

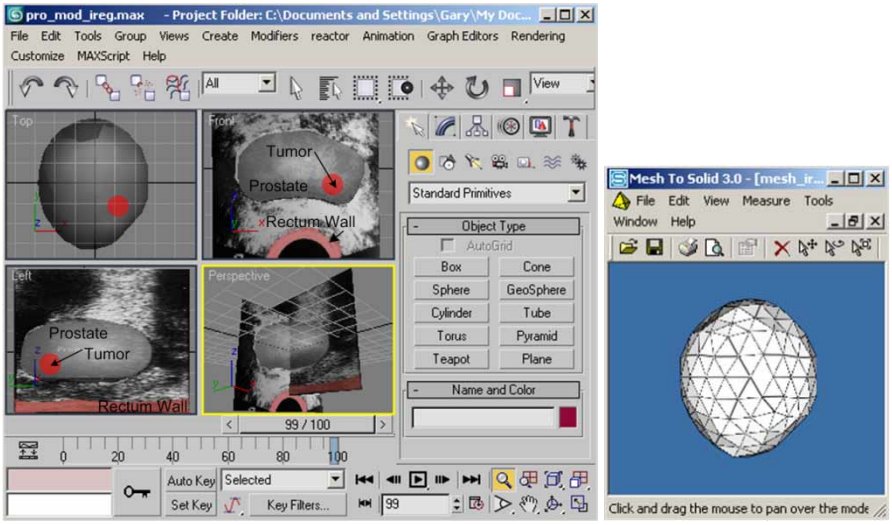


(a) (b)

Fig. 2. (a) 3ds-MAX Interface, (b) Mesh-to-Solid Interface

The mesh in Fig. 3 corresponds to a volume of 80×80×80 $mm^3$ and the 'walnut' shaped prostate has a dimension of 50×50×30 $mm^3$. The rectum wall is 4mm thick with a curvature radius of 80 mm. The choice of the curvature radius is due to the fact that the NIR array added to a TRUS probe may have a flat surface that would transform the rectum lumen to an

#99968 - $15.00 USD Received 8 Aug 2008; revised 13 Oct 2008; accepted 14 Oct 2008; published 15 Oct 2008

elliptical shape. A larger radius also gives more flexibility in handling the posterior prostate region within the mesh.

Although only the rectum wall is a physical boundary, treating the other 5 surfaces as physical boundaries (Robin type, Equ. 2) should have negligible effect upon the results as the lateral-medial and ventral-dorsal dimensions well exceed the potential path of photon propagation for the NIR array given in Fig. 1(c). The modulation frequency $\omega$ of the source in Equ. 1 is set at 100MHz, and 1% Gaussian noise is added to all forward calculations to form the measurement data.

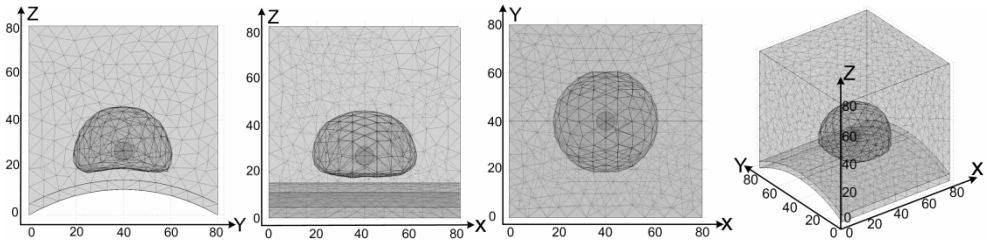


(a) Transverse View (b) Sagittal View (c) Coronal View (d) Perspective View

Fig. 3. FEM mesh generated based on approaches in Fig. 2. [Unit: mm].

## 3. A hierarchical spatial *prior* approach for trans-rectal NIR tomography reconstruction

### *3.1 Sensitivity of the sagittal trans-rectal NIR array*

The NIR array proposed in Fig. 1(c) has 7 source channels occupying one linear array and 7 detection channels occupying the other array. The sensitivity with respect to a perturbation of a specific optical property is determined by the corresponding Jacobian values in Equ. 3. Figure 4 plots the sensitivity specific to absorption, or $\partial \ln I_{ij} / \partial \mu_a$, for a medium with optical properties of $\mu_a = 0.01mm^{-1}$ and $\mu_s^{'} = 1.0mm^{-1}$, calculated by projecting the Jacobian values along a line in the imaging volume. Figure 4(a) is the longitudinal sensitivity in the mid-sagittal plane for a line from (0, 40, 30) to (80, 40, 30), Fig. 4(b) is the lateral sensitivity in the mid-transverse plan for a line from (40, 0, 30) to (40, 80, 30), and Fig. 4(c) is the depth sensitivity in the mid-sagittal plane for a line from (40, 40, 15.1) (here 15.1 is the $z$ coordinate, but the actual depth from the rectum surface is 0mm owing to the curvature of the rectum) to (40, 40, 80), respectively. The dimension or the locations of the source & detector array is marked on the abscissa of all three plots. The TRUS sagittal plane is located at y=40mm, which is the mid-sagittal plane within the NIR imaging volume.

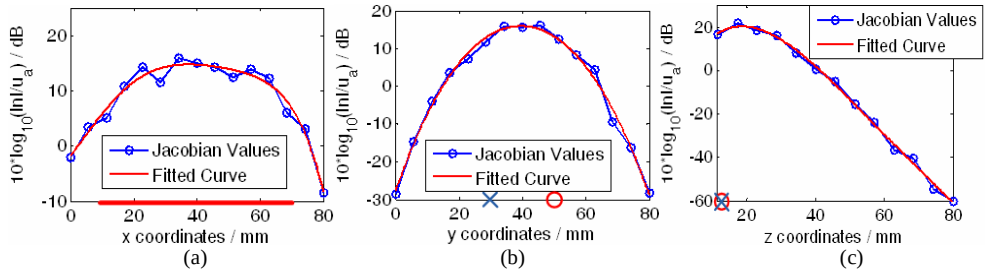


Fig. 4. Sensitivity profile. (a) Mid-sagittal plane, longitudinal sensitivity; (b) mid-transverse plane, lateral sensitivity; (c) mid-saggital plane, depth sensitivity. The marks on abscissa or the origin show the positions of optodes.

Figure 4 indicates that the longitudinal sensitivity has ~6dB variation in the middle 75% range of the array, and the lateral sensitivity peaks at the mid-saggital plane. In the middle-

#99968 - $15.00 USD Received 8 Aug 2008; revised 13 Oct 2008; accepted 14 Oct 2008; published 15 Oct 2008

sagittal plane the sensitivity degrades ~1dB/mm as z-coordinate increases from 20mm, which is apparently due to the side-way placement of the NIR array. The depth-degrading sensitivity will cause deeper targets to be reconstructed at a shallower position [28] if no spatial *prior* is incorporated.

### *3.2 Trans-rectal NIR image reconstruction without a priori information*

The performance of recovering tumor-mimicking target by trans-rectal NIR tomography without any structural *prior* is examined. Figure 5 lists the results for the tumor target being placed at left, middle, and right within the prostate. The top row in Fig. 5 lists the target images of $\mu_a$ and $\mu_s^{'}$ generated by the TRUS-defined geometry as shown in Fig. 3. The optical properties of the 10mm diameter tumor target are $\mu_a = 0.02mm^{-1}$ and $\mu_s^{'} = 1.6mm^{-1}$, with the parameters of other regions as listed in Table 1. These target images are used to generate the noise-added simulated measurement data. The image reconstruction is then conducted using a mesh of homogenous element density throughout the entire volume and updated element by element. The results are given in the bottom row of Fig. 5. As seen, the tumor target may be localized, but the recovered resolution or spatial information is poor. The accuracy of optical property recovery is also low. Further, it is found that a tumor target with negative contrast in absorption cannot be accurately recovered using similar settings. It is however expected that the detection and characterization of the tumor target will be improved when the spatial information of prostate and the tumor is available.

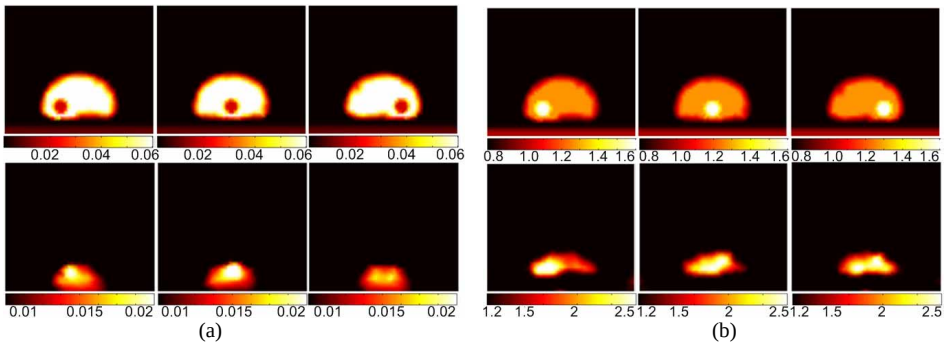


Fig. 5. NIR-only element-based reconstruction of a tumor target in various longitudinal locations. Row 1: target image for calculating the forward data; Row 2: Images reconstructed without any spatial prior. (a): $\mu_a$ images; (b): $\mu_s^{'}$ images. [Unit: $mm^{-1}$]

### *3.3 A hierarchical spatial prior method for TRUS guided trans-rectal NIR reconstruction*

The tissue volume interrogated by trans-rectal NIR imaging constitutes a nested-domain including a thin layer of rectum wall, a large volume of peri-prostate tissue, a relatively absorbing prostate, and the lesion within the prostate. These nested imaging domains may be further complicated by the pelvic bone that could interfere with the light propagation. Schweiger, et al. [38], Kolehmainen et al. [39-41], and Srinivasan et al. [42] have previously investigated the issue of recovering the shapes and optical properties of regions with optical contrast inside a non-nested or nested domains, where the shapes of the ROIs were derived from optical information when no spatial *prior* is available from other complementary imaging modalities. These methods have shown sufficient robustness in recovering the shapes and optical properties of the ROIs, yet the problem of stability and/or slow convergence was noticed in such approaches dealing with nested-domains. In trans-rectal NIR tomography reconstruction the spatial information from TRUS may be implemented by assigning homogenous optical properties within each ROIs of the imaging domain. However the convergence and the accuracy of reconstruction will still depend upon the initial guess in

#99968 - $15.00 USD Received 8 Aug 2008; revised 13 Oct 2008; accepted 14 Oct 2008; published 15 Oct 2008

addition to the accuracy of the *prior* information. The dependence on initial guess in a gradient based solver is due to the local minimum feature [36], as indicated in Fig. 6, which could be exaggerated in prostate imaging due to the possible multiple combinations of optical properties in the nested-structures. The image reconstruction in trans-rectal optical tomography is further complicated by the discrepancy regarding the optical contrast that the prostate tumor could have, namely positive or negative [19-22, 27].

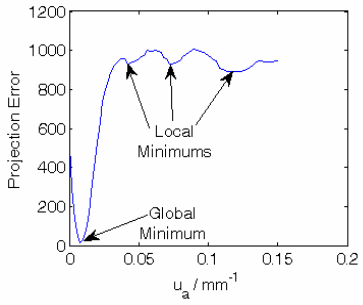


Fig. 6. Local-minimum issue in reconstruction. The forward calculation is based on Fig. 3(a) with assumption of homogeneous imaging volume. The projection error is calculated by using reduced scattering coefficient of the true value (0.008mm$^{-1}$), and using an absorption coefficient value from 0 to 0.15mm$^{-1}$ at a step of 0.002mm$^{-1}$, with respect to the forward data. Other than the global minimum, three local minimums can be observed where the iteration can stop incorrectly. This is the effect of varying only one parameter. More local minimums may occur when reconstructing more parameters.

When the TRUS is available, a conventional method of utilizing the spatial information would be the having the optical property of each ROI set as homogenous and updated simultaneously at each iteration. However, we have found that this conventional approach may not lead to reliable convergence for prostate imaging, which is attributed to the local-minimum problem. One example is given in Table 1 for the NIR array shown in Fig. 1(c). The prostate model is generated according to a previous work [27] (details of which are given later in Fig. 8), and a target of 10mm diameter is located at (40, 50, 15) which is 15 mm from the rectal surface. When the four ROIs including the rectum, the peri-prostate tissue, the prostate, and the prostate tumor are updated simultaneously from the same initial guess of $\mu_a$ =0.01mm$^{-1}$ and $\mu_s'$ =1.0mm$^{-1}$, the iteration stops after 1 update due to the negative $\mu_a$ value obtained for the rectum wall. The iteration fails to continue apparently due to the local minimum issue.

Table 1. Results of simultaneously updating the 4 ROIs from the same initial guess

| | $\mu_a$ (mm$^{-1}$) | | | | $\mu_s'$ (mm$^{-1}$) | | | |
|---|---|---|---|---|---|---|---|---|
| Regions | Surrounding Tissue | Rectum Wall | Prostate | Tumor | Surrounding Tissue | Rectum Wall | Prostate | Tumor |
| Set value | 0.002 | 0.01 | 0.06 | 0.02 | 0.8 | 1 | 1.27 | 1.6 |
| Simultaneous Update | 0.1216 | **-0.008** | 0.026 | 0.0215 | 1.1482 | 2.3602 | 0.6173 | 0.7073 |

The local minimum problem may be mitigated by a cascaded initial-guess approach or a hierarchical spatial *prior* method. The principle of this method is to first reconstruct the global optical properties of the entire volume, then to reconstruct the optical properties of prostate and rectum wall, and last to reconstruct the tumor lesion area. The 2$^{nd}$ and 3$^{rd}$ steps use the value obtained in the previous step as the initial guess of that specific ROI. Therefore at each step, the perturbation by a relatively smaller region is less influential and convergence of the iteration is better achieved. The detailed steps are shown in Fig. 7 and described in below:

#99968 - $15.00 USD Received 8 Aug 2008; revised 13 Oct 2008; accepted 14 Oct 2008; published 15 Oct 2008

(a) The first iterations assign an entirely homogenous imaging volume. In this round the initial projection error will be large and the convergence is most likely dominated by the global minimum. A single set of $\mu_a$ and $\mu_s'$ are determined using LM algorithm (Equ. 4) and will be used as the initial guess for the second step.

(b) The second iterations consider three regions, the rectum wall, peri-prostate tissue, and prostate, within the imaging volume. The calculation of the optical properties of these three ROIs start at the same initial guess as provided in step (a) but converges at different values.

(c) The values obtained from step (b) are used as the initial guess for the three ROIs but with a tumor added to the prostate. The tumor and the prostate take the same initial values as determined by the previous step. Each of the four ROIs (rectum wall, peri-prostate tissue, prostate, and tumor) converge to different end value.

The change of the overall projection error for the three steps is plotted in Fig. 7(d), and as evident, rapid and reliable convergence is observed. The hierarchy of the implementation of initial values for iteration is illustrated alternatively in Fig. 7(e).

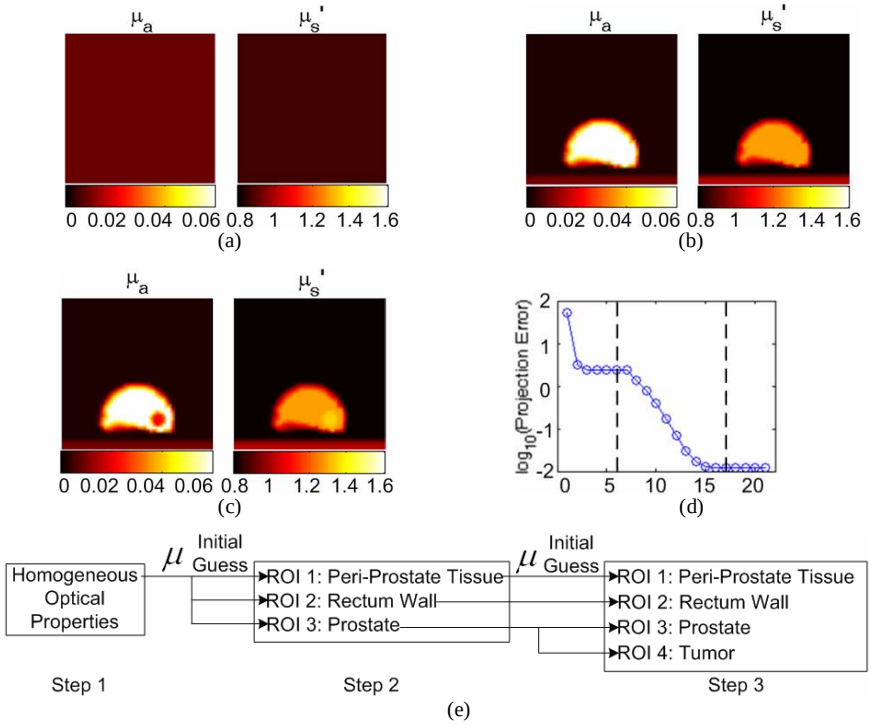


Fig. 7. The 3-step hierarchical reconstruction method (a) Step 1—one ROI for the entire volume; (b) step 2—three ROIs representing rectum wall, peri-prostate tissue, prostate; (c) step 3—four ROIs representing rectum wall, peri-prostate tissue, prostate, tumor; (d) change of the overall projection error, where the dash lines separate the converging of the three steps in (a)—(c); (e) block chart of the hierarchical initial guess assignment. [Unit in (a)---(c): $mm^{-1}$]

### *3.4 Validation of the hierarchical spatial prior method*

Recently Li et al. reported simulation results for trans-rectal optical tomography in the context of using MRI anatomic information [27], which is referred to as "NIR/MRI" in the following text. The proposed hierarchical spatial *prior* method is evaluated using the same probe geometry, prostate geometry and the optical properties (also in Table 1) presented in the NIR/MRI work. The size and depth of the tumor for simulation were not specified in the NIR/MRI work, but a tumor with diameter of 10 mm and a depth of 15mm from the planar probe surface is considerably close to the one presented in the NIR/MRI paper. The NIR/MRI

#99968 - $15.00 USD Received 8 Aug 2008; revised 13 Oct 2008; accepted 14 Oct 2008; published 15 Oct 2008

work also indicated the challenge of reconstruction that may be due to the local minimum. The authors set an arbitrary searching range for the optical properties ($\mu_a$:0-0.1 $mm^{-1}$, $\mu_s'$:0-2 $mm^{-1}$), and in 4 sets of the results, 3 of the tumor absorption value reached the limits and were stopped from further iteration, whereas the 4th value converged at a value more than 2 folds of the set value.

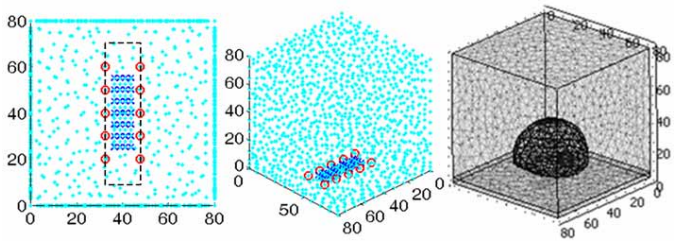

(a) (b) (c)

Fig. 8. The FEM mesh generated by following the geometry in NIR/MRI paper: (a) the geometry of the optodes, where the dash rectangle delineates the dimension of the NIR array that will be evaluated later for integration with US; (b) the 3-d view of the optodes and the imaging volume; (c) FEM containing the prostate and the tumor. [Unit: mm]

In the NIR/MRI work, a stand-alone trans-rectal NIR probe is simulated. The stand-alone NIR probe could have contained more optode channels incorporated than a TRUS-coupled NIR probe. In the NIR/MRI work, the best result is deducted for 10 sources and 28 detectors, which is used to evaluate the hierarchical method. The NIR probe geometry and the imaging domain of the NIR/MRI work are re-plotted in Fig. 8 for clarification and the hierarchical method is also preformed in transverse-view as did the NIR/MRI work. A 1% noise is also used in both methods assuring the consistency of measurement data.

Table 2. Reconstruction of a prostate tumor of negative contrast with respect to the prostate

| | $\mu_a$ (mm$^{-1}$) | | | | $\mu_s'$ (mm$^{-1}$) | | | |
|---|---|---|---|---|---|---|---|---|
| Regions | Surrounding Tissue | Rectum Wall | Prostate | Tumor | Surrounding Tissue | Rectum Wall | Prostate | Tumor |
| Set value | 0.002 | 0.01 | 0.06 | 0.02 | 0.8 | 1 | 1.27 | 1.6 |
| NIR/MRI | 0.0025 | 0.01 | 0.0575 | 0.0448 | 0.8324 | 1 | 1.339 | 1.075 |
| 3-step | 0.002 | 0.0099 | 0.06 | 0.0208 | 0.8012 | 1.0028 | 1.2824 | 1.3495 |

Table 3. Reconstruction of a prostate tumor of positive contrast with respect to the prostate

| | $\mu_a$ (mm$^{-1}$) | | | | $\mu_s'$ (mm$^{-1}$) | | | |
|---|---|---|---|---|---|---|---|---|
| Regions | Surrounding Tissue | Rectum Wall | Prostate | Tumor | Surrounding Tissue | Rectum Wall | Prostate | Tumor |
| Set value | 0.002 | 0.01 | 0.006 | 0.02 | 0.8 | 1 | 1.27 | 1.6 |
| 3-step | 0.0020 | 0.0100 | 0.0061 | 0.0163 | 0.7998 | 0.9997 | 1.2863 | 1.2434 |

Table 2 lists the results of the hierarchical method in comparison with those given in NIR/MRI paper. The hierarchical method (listed as "3-step" in the table), as expected, slightly outperforms the NIR/MRI method in terms of the accuracy of recovering optical properties. The results of recovering a target of positive absorption contrast are listed in Table 3 using the NIR/MRI probe geometry and our proposed 3-step method. The case of reconstructing a target with positive absorption contrast is not presented in the NIR/MRI paper, therefore only

#99968 - $15.00 USD Received 8 Aug 2008; revised 13 Oct 2008; accepted 14 Oct 2008; published 15 Oct 2008

the 3-step method is presented in Table 3 for comparison with the set values. In Table 3 the absorption coefficient of prostate is set much lower than that in Table 2 but the tumor optical properties are kept the same as those in Table 2. It is found that if the absorption of prostate in Table 3 is kept the same as in Table 2, the positive absorption target can hardly be reconstructed. The choice of lower prostate absorption is for testing our hierarchical method and the values may be much lower than the values reported of prostate [19-22]. It is noted that the reported values of prostate absorption coefficient vary in literatures where the measurements were taken either from *in vitro* tissue or from *in vivo* tissue using invasive methods. The absorption coefficient of intact or native prostate is in fact unknown, and is likely to be lower than the values reported in literatures.

The reconstructed images for targets of both negative and positive contrasts are listed in Fig. 9. These results demonstrate the capability of our hierarchical spatial *prior* method in reconstructing prostate lesion with either negative or positive absorption contrast.

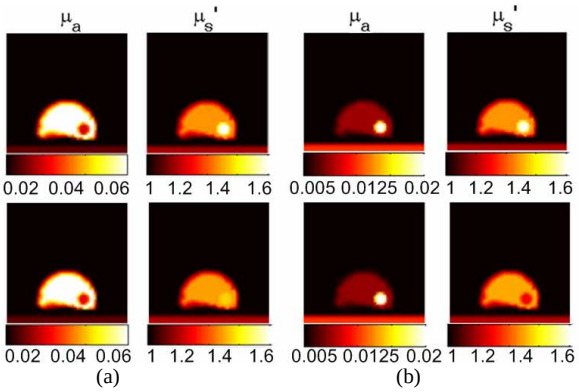


Fig. 9. Reconstructed images for a target with absorption contrast: (a) negative contrast (b) positive contrast. Top row: target setting; Bottom row: reconstructed image. [Unit: $mm^{-1}$]

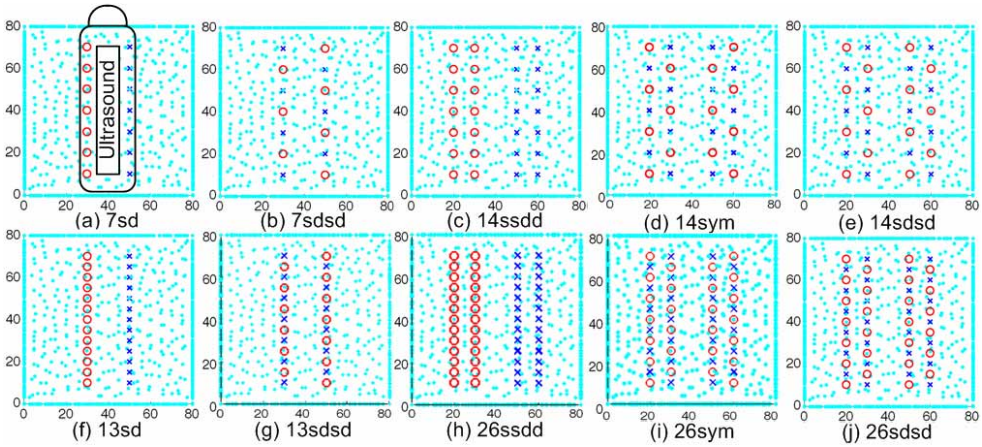


Fig. 10. NIR array designs. The dimension of the sagittal TRUS is shown in (a). The number of the Fig. caption denotes the number of opdotes on each lateral side of the TRUS as is depicted in (a). "sd" denotes one line of source and one line of detector; "ssdd" denotes two lines of source and two lines of detector; "sdsd" denotes mixed source/detector in one line; "sym" denotes symmetric distribution of the optodes with respect to the sagittal TRUS. [Unit: mm]

#99968 - $15.00 USD Received 8 Aug 2008; revised 13 Oct 2008; accepted 14 Oct 2008; published 15 Oct 2008

## 4. Assessment of NIR applicator designs for coupling NIR with TRUS

It is stated previously that an NIR array of dual-line geometry is feasible for concurrent trans-rectal NIR/US imaging considering the space limitation when coupling NIR with TRUS transducer for endo-rectal application. Based on the fabrication constraints, we have also suggested that each line array consist of 7 channels. The 7 channels could be exclusively source or detector as shown in Fig. 10(a), or interspersed source/detector as in Fig. 10(b). There are certainly a number of NIR geometries that can be coupled to TRUS sagittal transducer if not-limited by difficulties in fabrication or endo-rectal use. Compared with the geometry in Fig. 10(a), more channels could be added to each line-array as shown in Fig. 10(f), more lines can be added as shown in Fig. 10(c), or more lines and more channels added as in Fig. 10(h). More options are also listed in Fig. 10.

The array in Fig. 10(a) is the most desirable in terms of the fabrication easiness and endo-rectal applicability. The designs in Fig. 10(a), (b), (f) and (g) correspond to an NIR probe with a minimum lateral dimension of 20mm. The designs in Fig.10(c)-(e) and (h-j) correspond to NIR probe with a minimum 40mm lateral dimension which is not suitable for endo-rectal use. The geometries in Fig. 10(a)—(e) represent a 10mm spacing between the closest optodes, and the geometries in Fig. 10(f)—(j) require a 5mm spacing between the closest optodes. The smaller spacing in Fig. 10(f)—(j) will be challenging for fabrication considering the number of fiber channels and the side-firing configuration if the probe is to be integrated to TRUS probe unless the internal structural of the TRUS probe can be altered.

### *4.1 Sensitivity comparison*

The sensitivities of all the 10 configurations of Fig. 10 are compared in Fig. 11. The mesh in Fig. 3 with homogeneous optical properties ($\mu_a = 0.01mm^{-1}$ and $\mu_s^{'} = 1.0mm^{-1}$) is used for the sensitivity calculation. The sensitivity in Fig. 10 is evaluated at the lines identical to those in Fig. 4. Only the absorption sensitivity is evaluated.

The observations made from Fig. 11 are: (1) increasing the spatial dimension of source-detector array generally improves the sensitivity; (2) increasing the number of source-detector pairs generally improves the sensitivity, as demonstrated previously [43]; (3) interspersed source-detector layout may have slightly wider lateral sensitivity but is comparable to non-dispersed source-detector layout for other imaging views; (4) the geometry of 26ssdd (the upper thicker line) has the best sensitivity feature among the 10 geometries, therefore it can be used as a standard to evaluate the simple geometry of 7sd (the lower thicker line).

### *4.2 Comparison between the 7sd design and the 26ssdd design*

The 7sd design represents an array which is less challenging in fabrication and more practical for endo-rectal use. The 26ssdd geometry is impractical for endo-rectal application, difficult to fabricate, but has the best performance among the designs listed. It is shown in Fig. 11 that the sensitivity of 7sd design is approximately 10dB lower than that of 26ssdd in the specified longitudinal, lateral, and depth directions. Quantitative comparison of the performance is conducted between these two geometries for representative target variations. The optical properties listed in Table 2 (set values) are used for these comparisons.

#99968 - $15.00 USD Received 8 Aug 2008; revised 13 Oct 2008; accepted 14 Oct 2008; published 15 Oct 2008

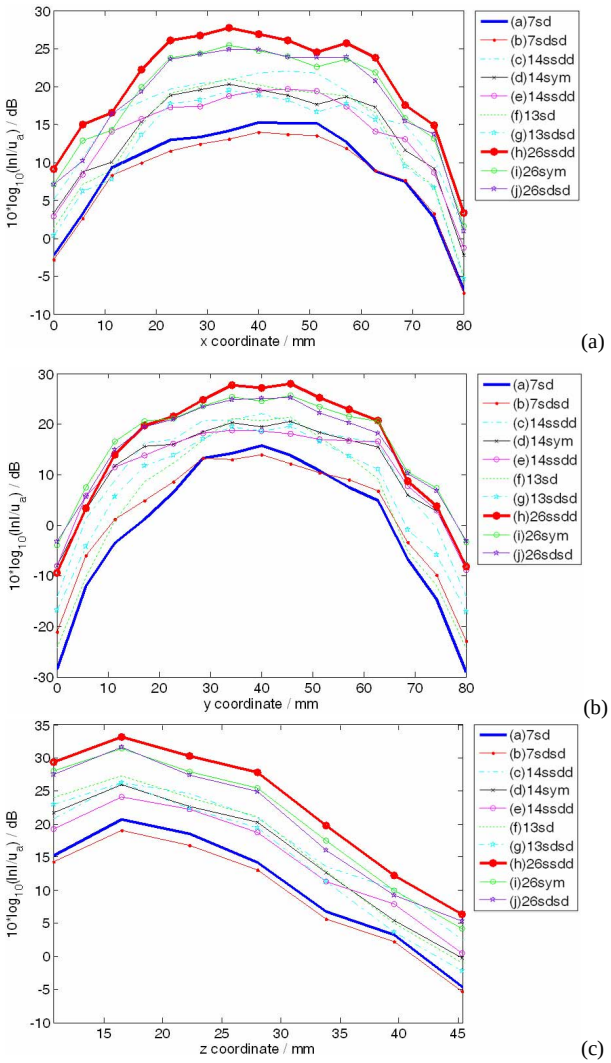


Fig. 11 Sensitivity comparison: (a) longitudinal direction, (b) lateral direction, (c) depth direction. The upper thicker line corresponds to the configuration (h) in Fig. 10, and the lower thicker line corresponds to the desired configuration (a) in Fig. 10.

### *4.2.1 Reconstruction accuracy versus target longitudinal location*

A target of 10mm in diameter is placed at the middle-sagittal plane of y=40mm, z=26mm, and varied in longitudinal coordinates from x=25 to 55mm with a step of 5mm (Fig. 12(a)). The optical properties reconstructed by the two geometries are plotted versus the true values in Fig. 12(b) and (c). The optical properties recovered by 26ssdd and 7sd designs are close to each other at most of the longitudinal locations, but the 7sd design shows a larger variation in the recovered absorption contrast at x=30mm and x=50mm compared to other positions. This may be related to fewer source-detector pairs that contribute to the target detection when close to the boundary or the existence of any irregular elements in the mesh.

#99968 - $15.00 USD Received 8 Aug 2008; revised 13 Oct 2008; accepted 14 Oct 2008; published 15 Oct 2008

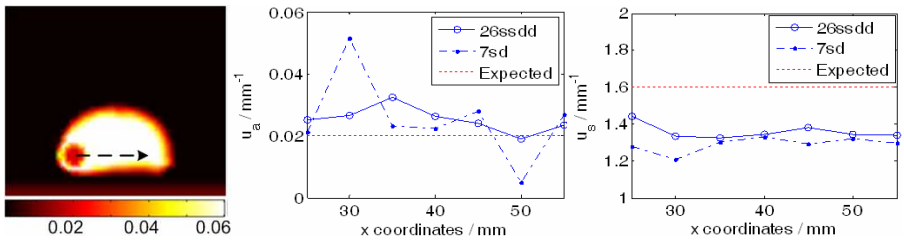


(a) (b) (c)

Fig. 12. Comparison of two geometries for a target varying in longitudinal location in the middle-sagittal plane: (a) illustration of the target location change [Unit: mm$^{-1}$]; (b) comparison of absorption coefficient reconstruction; (c) comparison of reduced scattering coefficient reconstruction

### *4.2.2 Reconstruction accuracy versus target depth*

A target of 10mm in diameter is placed at the middle-sagittal plane at x=40mm, y=40mm, and the depth is varied from z=25 to 40mm at a step of 2.5mm (the last data point is simulated at z=39mm as at 40mm the target is out of the prostate) (Fig. 13(a)). The reconstructed optical properties are plotted in Fig. 13(b) and (c). The 26ssdd configuration outperforms the 7sd one again, however beyond z=30mm, both designs are incapable of recovering the absorption coefficient of the target from the prostate background. This depth limitation is related to the maximum span of the NIR array, the absorption coefficient of the prostate, and the size of the target. For a larger target with a diameter of 14mm, it is verified that the target may be resolved up to 36mm depth from the NIR array in comparison to 30mm for a target of 10mm diameter. A potentially smaller absorption coefficient of intact prostate may also increase the depth limit of target detection due to an increase in sensitivity.

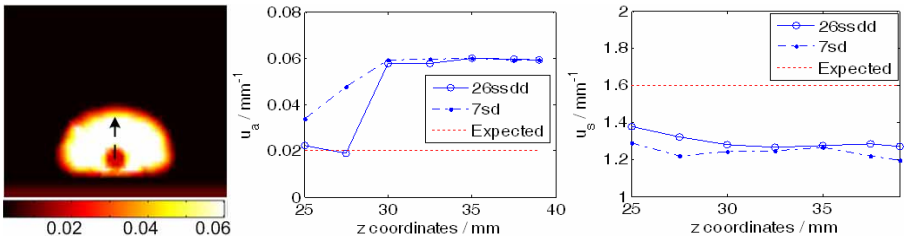


(a) (b) (c)

Fig. 13. Comparison of two geometries for a target varying in depth in the middle-sagittal plane: (a) illustration of the target location change [Unit: mm$^{-1}$]; (b) comparison of absorption coefficient reconstruction; (c) comparison of reduced scattering coefficient reconstruction

### *4.2.3 Reconstruction accuracy versus target size*

A target is placed at middle-sagittal plane of x=40mm, y=40mm and z=26mm, and the diameter is varied from 4mm to 14mm with a step of 1mm. The target diameter change is illustrated in Fig. 14(a). The reconstructed optical properties are shown in Fig. 14(b) and (c). It is clear that the larger the target, the better the accuracy of reconstruction. The 26ssdd can recover the absorption contrast of the target when the diameter is greater than 6mm and the 7sd can recover the target for target diameter greater than 8mm.

These comparisons suggest that the 7sd design is inferior to the 26ssdd design, especially for the reconstruction of absorption properties. However, the accuracy of reconstructing scattering properties by the 7sd design is close to that of 26ssdd. Considering the challenges in trans-rectal NIR probing for coupling with TRUS, it is fair to develop and test the instrumentation with the 7sd design.

#99968 - $15.00 USD Received 8 Aug 2008; revised 13 Oct 2008; accepted 14 Oct 2008; published 15 Oct 2008

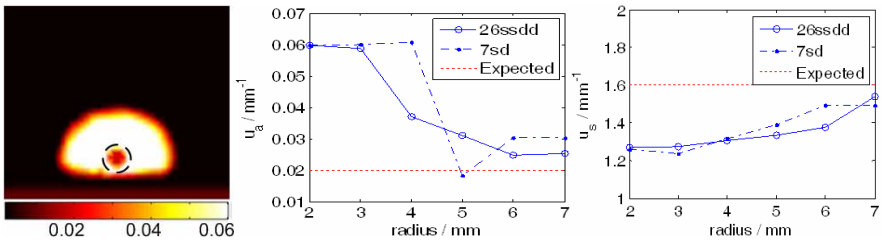


(a) (b) (c)

Fig. 14. Comparison of two geometries for a target varying in size in the middle-sagittal plane: (a) illustration of the target size change [Unit: $mm^{-1}$]; (b) comparison of absorption coefficient reconstruction; (c) comparison of reduced scattering coefficient reconstruction

### *4.3 Capability of recovering two targets by the 7sd design in sagittal plane*

Capability of differentiating two targets is of particular relevance to prostate cancer imaging owing to the existence of secondary or multifocal tumors [44-46]. The multiple lesions may fall into the same TRUS field-of-view (FOV), or one falls outside the TRUS FOV. For the former case, the US *prior* could be used to guide NIR reconstruction of both targets. For the latter case, as NIR actually performs 3-D imaging it may interrogate the out-of-plane target and help redirecting the US to that target. In this section, however, we investigate only the former case of having two targets in the same sagittal plane. This requires implementing the multi-target location information in the last step of the hierarchical spatial *prior* routine. The following simulations are conducted with the 7sd probe design only.

#### *4.3.1 Reconstruction of two targets located at the same depth in sagittal plane*

Figure 15 shows two 10mm-diameter regions being added to the prostate, at coordinates (25, 40, 26) and (55, 40, 26), respectively. In Fig. 15(a) only one region has optical contrast, and in Fig. 15(b) both regions have optical contrasts. In both cases the optical contrast can be reconstructed with good accuracy, as is shown in Table 4. The $\mu_a$ of the target with true optical contrast is reconstructed within ±20% of the set value and $\mu_s'$ can be reconstructed within ±23% of the set values. The target with no optical contrast is reconstructed with some artifacts, nevertheless, the target with optical contrast can be easily differentiated from the one without.

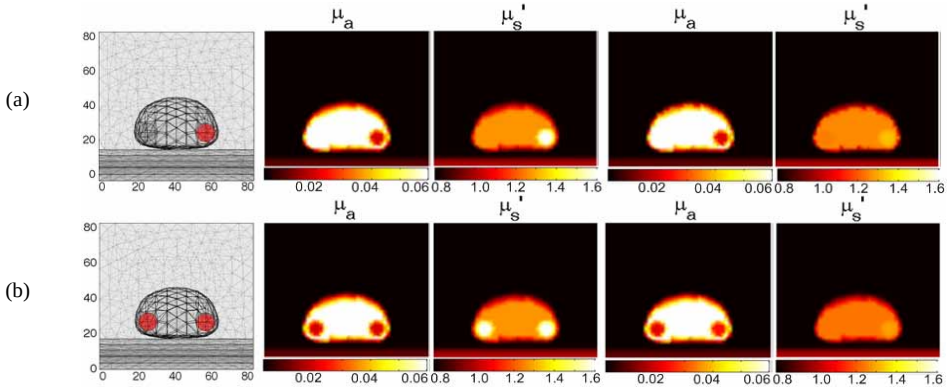


Fig. 15. Two suspicious regions at the same depth [Units: mm and $mm^{-1}$]

#99968 - $15.00 USD Received 8 Aug 2008; revised 13 Oct 2008; accepted 14 Oct 2008; published 15 Oct 2008

Table 4. Comparison of reconstructed optical properties ($mm^{-1}$) in Fig. 15

| $\mu_{a(mm^{-1})}$ | | | | | | |
|---|---|---|---|---|---|---|
| Fig. | Regions | Peri-prostate | Rectum | Prostate | Target 1 | Target 2 |
| (a) | Set value | 0.002 | 0.01 | 0.06 | 0.06 | 0.02 |
| | Reconstructed | 0.002 | 0.0101 | 0.0601 | 0.0778 | 0.0208 |
| (b) | Set value | 0.002 | 0.01 | 0.06 | 0.02 | 0.02 |
| | Reconstructed | 0.002 | 0.01 | 0.0597 | 0.0207 | 0.024 |
| $\mu_s'$ $(mm^{-1})$ | | | | | | |
| Fig. | Regions | Peri-prostate | Rectum | Prostate | Target 1 | Target 2 |
| (a) | Set value | 0.8 | 1.0 | 1.27 | 1.27 | 1.6 |
| | Reconstructed | 0.7995 | 0.9935 | 1.261 | 1.2187 | 1.3216 |
| (b) | Set value | 0.8 | 1.0 | 1.27 | 1.6 | 1.6 |
| | Reconstructed | 0.8007 | 0.9953 | 1.2343 | 1.2302 | 1.2837 |

### *4.3.2 Reconstruction of two targets located at different depth in sagittal plane*

Two targets of 10mm diameter are added in the prostate at coordinates of (25, 40, 28) and (55, 40, 24), respectively. Figure 16 shows the reconstructed images for the case of both targets having negative contrast and the reconstructed values are listed in Table 5.

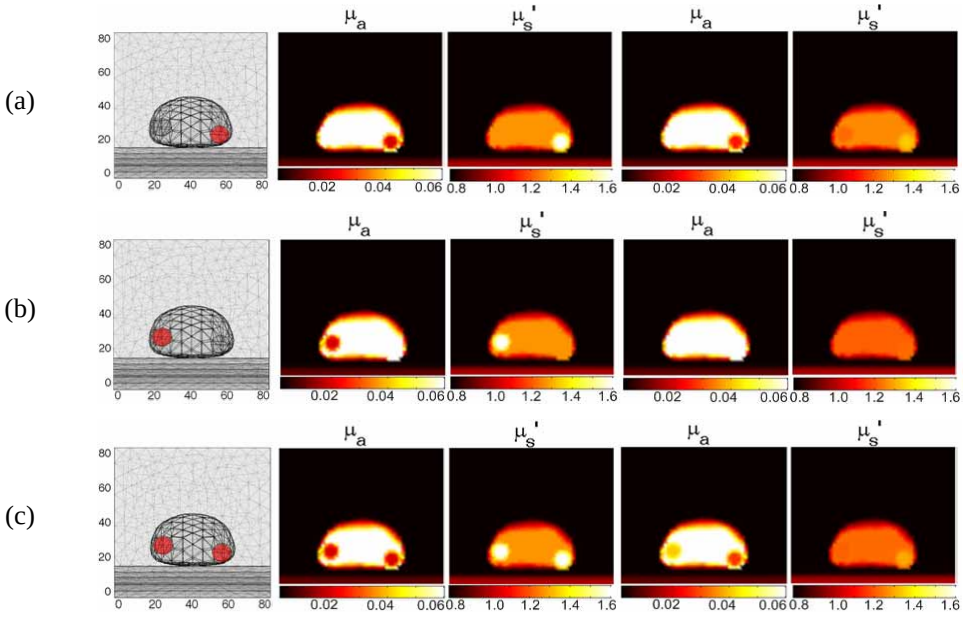


Fig. 16. Two targets at different depths: negative contrast cases [Unit: mm and $mm^{-1}$]

#99968 - $15.00 USD Received 8 Aug 2008; revised 13 Oct 2008; accepted 14 Oct 2008; published 15 Oct 2008

Table 5. Comparison of reconstructed optical properties ($mm^{-1}$) in Fig. 16

| $\mu_a$ ($mm^{-1}$) | | | | | | |
|---|---|---|---|---|---|---|
| Fig. | Regions | Peri-prostate | Rectum | Prostate | Region 1 | Region 2 |
| (a) | Set value | 0.002 | 0.01 | 0.06 | 0.06 | 0.02 |
| | Reconstructed | 0.002 | 0.01 | 0.0594 | 0.0674 | 0.0252 |
| (b) | Set value | 0.002 | 0.01 | 0.06 | 0.02 | 0.06 |
| | Reconstructed | 0.002 | 0.0101 | 0.0597 | 0.0592 | 0.0607 |
| (c) | Set value | 0.002 | 0.01 | 0.06 | 0.02 | 0.02 |
| | Reconstructed | 0.002 | 0.01 | 0.0596 | 0.0402 | 0.0276 |
| $\mu_s'$ ($mm^{-1}$) | | | | | | |
| Fig. | Regions | Peri-prostate | Rectum | Prostate | Region 1 | Region 2 |
| (a) | Set value | 0.8 | 1.0 | 1.27 | 1.27 | 1.6 |
| | Reconstructed | 0.8009 | 0.9977 | 1.2538 | 1.2167 | 1.3286 |
| (b) | Set value | 0.8 | 1.0 | 1.27 | 1.6 | 1.27 |
| | Reconstructed | 0.8015 | 0.9931 | 1.2102 | 1.2179 | 1.2083 |
| (c) | Set value | 0.8 | 1.0 | 1.27 | 1.6 | 1.6 |
| | Reconstructed | 0.8015 | 0.9956 | 1.2177 | 1.2024 | 1.2962 |

When the target is at a depth of 24mm, the $\mu_a$ and $\mu_s'$ can be reconstructed within ±20% and ±25% of the set values, respectively. However, a target at 28mm depth cannot be reconstructed. This is due to the prostate's high absorption coefficient of $0.06mm^{-1}$. When the prostate absoption coefficient is reduced to $0.006mm^{-1}$ which will provide positive optical contrast in the two target regions, both tartgets can be recovered as shown in Fig. 17 and Table 6. The $\mu_a$ of the target can be reconstructed within ±5% of the set value, while the $\mu_s'$ is still reconstructed within ±23% of the expected values.

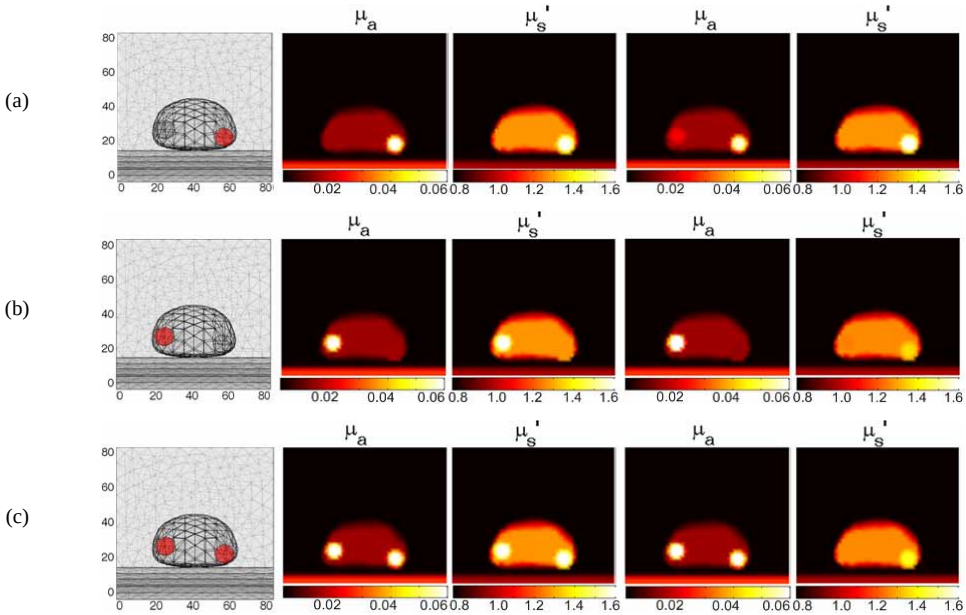


Fig. 17. Two targets at different depths: positive contrast cases [Unit: mm and $mm^{-1}$]

#99968 - $15.00 USD Received 8 Aug 2008; revised 13 Oct 2008; accepted 14 Oct 2008; published 15 Oct 2008

Table 6. Comparison of reconstructed optical properties ($mm^{-1}$) in Fig. 17

| $\mu_{a(mm^{-1})}$ | | | | | | |
|---|---|---|---|---|---|---|
| Fig. | Regions | Peri-prostate | Rectum | Prostate | Region 1 | Region 2 |
| (a) | Set value | 0.002 | 0.01 | 0.006 | 0.006 | 0.02 |
| | Reconstructed | 0.002 | 0.0101 | 0.006 | 0.0083 | 0.0191 |
| (b) | Set value | 0.002 | 0.01 | 0.006 | 0.02 | 0.006 |
| | Reconstructed | 0.002 | 0.0101 | 0.006 | 0.0116 | 0.0058 |
| (c) | Set value | 0.002 | 0.01 | 0.006 | 0.02 | 0.02 |
| | Reconstructed | 0.002 | 0.0099 | 0.006 | 0.0208 | 0.0199 |
| $\mu_s'$ $(mm^{-1})$ | | | | | | |
| Fig. | Regions | Peri-prostate | Rectum | Prostate | Region 1 | Region 2 |
| (a) | Set value | 0.8 | 1.0 | 1.27 | 1.27 | 1.6 |
| | Reconstructed | 0.7993 | 0.9934 | 1.2637 | 1.2689 | 1.6722 |
| (b) | Set value | 0.8 | 1.0 | 1.27 | 1.6 | 1.27 |
| | Reconstructed | 0.8008 | 0.993 | 1.259 | 1.2402 | 1.3586 |
| (c) | Set value | 0.8 | 1.0 | 1.27 | 1.6 | 1.6 |
| | Reconstructed | 0.8049 | 0.9979 | 1.2576 | 1.2538 | 1.424 |

## 5. Discussions

The scope of this work is to investigate the feasibility of trans-rectal NIR tomography of the prostate in the context of concurrent imaging with sagittal TRUS using combined endo-rectal NIR/US probe. Recently there have been considerable interests on trans-rectal NIR tomography to augment existing imaging modalities which cannot be validated without the development of an endo-rectal NIR applicator. With an endo-rectal applicator, trans-rectal NIR tomography of the prostate can be performed stand-alone. However, without a position correlation with a real-time anatomic imaging modality such as TRUS, the images obtained by trans-rectal NIR would be difficult to interpret. Combining the NIR applicator with TRUS is a viable solution for accurate positioning of the NIR probe which would further enable using TRUS anatomy to guide the image reconstruction of trans-rectal NIR tomography. A variety of designs of NIR array for coupling with TRUS are possible, however, the NIR probe dimension and the number of NIR channels on the probe are quite limited.

The utilization of a hierarchical spatial *prior* is under the condition that the anatomic information of the prostate tumor can be extracted explicitly from TRUS. The prostate boundary can be well-delineated in TRUS, and so does a strongly hypo-echoic region indicating a suspicious lesion. This is when the NIR imaging may help determine if the suspicious lesion is malignant or benign based on optical contrasts [31]. However, since as many as 40% of the tumors may be seen as iso-echoic on TRUS, the utility or accuracy of this hierarchical imaging approach is hindered when TRUS images do not specify a suspicious region, or when it is difficult to define the spatial extent of a suspicion region in TRUS. Under these circumstances, the third step of the proposed hierarchical image reconstruction routine may be performed by element-based reconstruction within the prostate instead of region-based reconstruction for the prostate. Such approach is proven effective based on our initial investigations, but the accuracy and robustness may be affected by the depth-dependent sensitivity of the endo-rectal NIR probe and the relatively small number of source/detector channels that may be engineered on the NIR probe. More dedicated investigations could be conducted when the trans-rectal NIR/US approach is experimentally demonstrated. Prostate trans-rectal optical imaging is a relatively new area, thus it is imperative to focus the initial approach of trans-rectal NIR/US on characterizing lesions identifiable on TRUS.

#99968 - $15.00 USD Received 8 Aug 2008; revised 13 Oct 2008; accepted 14 Oct 2008; published 15 Oct 2008

Characterizing lesions marginally suspicious to TRUS or iso-echoic on TRUS may become less-challenging when the knowledge on trans-rectal NIR tomography of lesions most suspicious on TRUS is available.

The simulations studies presented here are largely based on setting the absorption properties of prostate at a high level of $0.06mm^{-1}$. This is significantly larger than that of breast tissue, and it is this parameter that dominates the detection depth of trans-rectal NIR tomography for the NIR array being discussed. Recent studies indicate that improved measurement condition, such as suppressing the bleeding interference, may lead to a lower absorption value of the prostate [22]. If the prostate is measured at its intact or native states by modalities such as trans-rectal optical tomography, an even lower absorption coefficient of the prostate may be obtained. A lower absorption coefficient will allow the same NIR array to detect deeper targets. In fact, a TRUS-coupled trans-rectal NIR tomography may not only help characterize lesions suspicious to TRUS, but also help quantify the optical properties of intact prostate that are unavailable so far.

## 6. Conclusions

The feasibility of imaging the prostate using a TRUS-coupled NIR applicator is investigated by simulation. A hierarchical iteration algorithm is first developed in order to incorporate the TRUS spatial *prior* more reliably into the trans-rectal NIR image reconstruction. This hierarchical reconstruction method uses a cascaded initial-guess approach to mitigate the local minimum problem common to NIR tomography reconstruction. It is shown that trans-rectal optical tomography based on this method is reliable. This hierarchical reconstruction method is then utilized to evaluate a number of designs of NIR applicator that may be integrated with a sagittal TRUS transducer. A configuration of the endo-rectal NIR applicator is proposed, that contains single line of optode on each lateral side of the sagittal TRUS transducer, with 20mm lateral separation between the two line arrays and 10 mm longitudinal spacing among the total 7 channels on each line-array. The performance of this simple NIR array design is evaluated for the imaging of single tumor target in prostate by comparing with a much more complicated design that is impractical for endo-rectal application. The simple NIR array design is also evaluated for imaging of two targets in the prostate. Results suggest that trans-rectal imaging of the prostate is feasible by coupling this simple NIR array with TRUS.

The following Part-II paper presents the instrumentation of a TRUS-coupled endo-rectal NIR array and demonstrates trans-rectal optical tomography of the prostate by the combined endo-rectal NIR/US applicator. The endo-rectal NIR array has incorporated the design suggested by Fig. 10(a). Concurrent trans-rectal imaging is acquired in the same sagittal plane by both US and NIR optical tomography. The real-time TRUS is used for accurate positioning of the endo-rectal NIR applicator and for guiding NIR image reconstruction with the spatial *a priori* information. Tests on phantoms and tissues using the combined trans-rectal NIR/US imager demonstrate that optical contrast may be recovered by endo-rectal NIR imaging only but with improved accuracy when the TRUS spatial *prior* is incorporated. Trans-rectal imaging of a healthy canine prostate *in situ* administered with tissue contrast validates the endo-rectal utility of the NIR/US probe as well as the hierarchical method for TRUS guided trans-rectal NIR image reconstruction.

## Acknowledgments

This work has been supported by the Prostate Cancer Research Program of the U.S. Army Medical Research Acquisition Activity (USAMRAA), 820 Chandler Street, Fort Detrick MD, 21702-5014, through grant #W81XWH-07-1-0247. The content of the information does not necessarily reflect the position or the policy of the USARAA, and no official endorsement should be inferred. Comments and questions may be directed to Daqing Piao at daqing.piao@okstate.edu.

#99968 - $15.00 USD Received 8 Aug 2008; revised 13 Oct 2008; accepted 14 Oct 2008; published 15 Oct 2008